ADVANCED FUNCTIONAL MATERIALS
www.afm-journal.de

Quantum-Grade Nanodiamonds from a Single-Step, Industrial-Scale Pressure and Temperature Process

Yahua Bao, Michal Gulka, Parkarsh Kumar, Jakub Copak, Priyadharshini Balasubramanian, Yuliya Mindarava, Rémi Blinder, Michael Olney-Fraser, Haotian Wen, Hana Spanielova, Helen Zhi Jie Zeng, Benjamin Whitefield, Igor Aharonovich, Jaroslav Hruby, Fedor Jelezko, J. Daniel Belnap, Shery L. Y. Chang,* and Petr Cigler**

Nanodiamonds with nitrogen vacancy (NV) centers are a promising workhorse for myriad applications, from quantum sensing to bioimaging. However, despite two decades of extensive research, their use remains limited by the lack of scalable methods to produce quantum-grade material. While traditional NV-production methods involve multi-step irradiation and annealing processes, a fundamentally different approach is presented here based on a single-step high-temperature plastic deformation. It enables industrial-scale yield of high-quality luminescent nanodiamonds while significantly reducing production time and costs. Utilizing a unique cubic press apparatus capable of reaching higher temperatures and pressures, 50-nm luminescent nanodiamonds with outstanding optical and spin properties are achieved in a single step from non-luminescent material. Compared to electron-irradiated nanodiamonds, i.e., common commercially available material, this method yields NV centers with significantly improved charge stability, T_1 relaxation times approaching 1 ms, and a ≈5-fold enhancement in optical Rabi contrast. What this streamlined process produces in one week would require more than 40 years by current irradiation and annealing methods. Scalable, quantum-grade nanodiamonds are thus unlocked, providing the missing link for their widespread adoption.

1. Introduction

Nanoscale sensing using negatively-charged nitrogen vacancy centers (**NV**) in diamonds has achieved significant success and become a well-established field of research.[1] The NV electronic spin can be initialized, read, and coherently manipulated at room temperature while exhibiting long coherence times (≈ms),[2] making NV a key representative among solid-state qubits.[3,4] NV centers can also be incorporated into nanodiamonds (**NDs**),[5] which in turn enables the design of nanosized probes that report sensitively from the point of interest (e.g., biological environment) with submicrometer resolution.[6] This could include local detection of temperature changes[7,8] or specific molecules, for example, by employing NV spin relaxometry measurements.[9,10] However, despite two decades of extensive ND development starting in 2005[11] and followed by remarkable

Y. Bao, J. D. Belnap
MegaDiamond Technology Center
SLB Corporation
Provo, Utah 84606, USA
E-mail: dbelnap@slb.com

M. Gulka, J. Copak, H. Spanielova, P. Cigler
Institute of Organic Chemistry and Biochemistry of the CAS
Prague 166 10, Czech Republic
E-mail: petr.cigler@uochb.cas.cz

P. Kumar, H. Wen, S. L. Y. Chang
School of Material Science and Engineering
University of New South Wales
Sydney, NSW 2052, Australia
E-mail: shery.chang@unsw.edu.au

J. Copak
Department of Physical and Macromolecular Chemistry
Faculty of Science
Charles University
Hlavova 2030/8, Prague 2 128 40, Czechia

P. Balasubramanian, Y. Mindarava, R. Blinder, M. Olney-Fraser, F. Jelezko
Institute of Quantum Optics
Ulm University
89081 Ulm, Germany

H. Z. J. Zeng, B. Whitefield, I. Aharonovich
School of Mathematical and Physical Sciences
University of Technology Sydney
Ultimo
New South Wales 2007, Australia

The ORCID identification number(s) for the author(s) of this article can be found under https://doi.org/10.1002/adfm.202520907

DOI: 10.1002/adfm.202520907

progress in NV research,[12–16] there have been no widespread practical or commercial implementations of luminescent NDs.

Current synthetic methods are expensive and labor-intensive. The typical irradiation time for the creation of bright NDs for quantum sensing using an electron accelerator is 2 weeks (80 active h).[17] This limits their accessibility for broader use and wider commercial adoption. For example, chemical modifications required to prepare NV quantum nanosensors necessitate tens of milligrams of ND material, so the initial synthetic protocols are typically developed with non-luminescent NDs and re-optimized on their more expensive luminescent counterparts. Furthermore, current larger-scale synthesis methods produce NDs with NV spin relaxation times that are significantly shorter than those in larger diamond crystals. Therefore, the key to unlocking the full potential of luminescent NDs lies in improving the scalability and cost-efficiency of their synthesis, while providing superior NV spin properties.

NV-containing NDs are primarily made from high-pressure high-temperature (**HPHT**) diamonds[5] that contain single substitutional nitrogen defects ($\mathbf{N_s}$). To create NV centers, diamonds are irradiated with high-energy ions and annealed at high temperatures (>600 °C)[18,19] (**Figure 1**). Residual nitrogen impurities (P1 centers) contribute to NV decoherence and photoluminescence (**PL**) quenching,[14,20–22] making the initial nitrogen concentration and NV conversion yield critical. Optimizing the irradiation to balance vacancy creation with the avoidance of excessive damage is essential.[23–25] While certain irradiation types may be advantageous,[26–29] further studies are needed to quantify lattice damage and the consequential deterioration of NV spin properties. Some advances, such as rapid high-temperature annealing (**HTA**), have shown the potential to improve NV properties by healing lattice disorders in bulk and micro-sized diamonds.[30,31] However, HTA has not yet been effectively applied to sub-100 nm NDs,[32] likely due to material loss (graphitization) during processing. Currently, NVs in ≈50-nm sized HPHT NDs still exhibit approximately one-order-of-magnitude shorter T_1 and T_2 times compared to their bulk counterparts.

Here, we present a high-temperature plastic deformation method for NV creation, denoted as pressure & temperature qubits (**PTQ**) that circumvents these issues and replaces irradiation, annealing, and rapid HTA with a single-step procedure (Figure 1). It is a fast (≈minutes), high-yield (≈grams), and cost-effective alternative, designed for industrial-scale fabrication of quantum-grade NDs. The resulting ~50-nm particles show exceptional NV optical properties, namely a long T_1 time, remarkably high Rabi contrast, and two-fold increased NV^-/NV^0 ratio. In addition to NV red emission, these NDs contain green-emitting diamagnetic H3 (NVN) centers, which is unusual for this particle size range[32] and allows dual biolabelling inside cells. Most importantly, using just one modified commercial sintering press apparatus (as described below), our approach produces over 1 kg of high-quality fluorescent NDs per work week—a stark contrast to current approaches that produce gram levels per week at best and other emerging methods[33,34] with yields that are insufficient for practical applications.

2. Results

2.1. PTQ Method Yields High-Quality Fluorescent NDs

Our method relies on extremely high pressures (≈7 GPa) and temperatures (≈1700 °C) to create quantum-grade NV qubits in ≈50 nm ND. This pressure- and temperature-driven process enables the formation of vacancies without structurally damaging the ND lattices and surfaces (see below). This builds on the previous work of T. Evans et al.,[35] who observed the creation of NV and H3 centers in sintered micron-sized diamonds, which was attributed to diamond plastic deformation during the HPHT sintering process. The synthetic process relies on the formation of C vacancies, which, combined with increased nitrogen mobility at higher temperatures, leads to NV center creation. The deformation mechanisms are enabled by: 1) very large contact pressures of up to 30x the applied pressure developed between the diamond particles[36] and 2) higher temperatures allowing the onset of significant diamond plasticity in type Ib diamonds at ≈730 °C and full plasticity without fracture at temperatures over 1400 °C.[37] Recently we disclosed,[38,39] that subjecting type Ib NDs to high pressure and temperature conditions activates mechanisms that promote NV & H3 formation, while simultaneously enabling diamond thermodynamic stability at high temperature. Although high pressure might not be necessary for defect creation, as demonstrated recently,[40] it allows for diamond processing within the diamond-stable region.

To create PTQ NDs, we used a unique capsule with modifications enabling higher temperatures and pressures than are commonly employed in the diamond industry[41,42] (**Figure 2a**). This capsule operates within a cubic press apparatus, which is commonly used for diamond crystal synthesis and sintering.[43] However, our approach involves a departure from standard protocols for the preparation of sintered diamond materials, in which cobalt and nickel are employed as solvent catalysts.[35,44] Instead, we add diamagnetic sodium chloride to deliberately inhibit sintering.[39] After pressure p_A = 7 GPa is applied during initial heating, premixed solid sodium chloride applies semi-hydraulic pressure on some non-contact surfaces (p_{NC}) to help prevent graphitization.[39] In regions of direct diamond-diamond

B. Whitefield
ARC Centre of Excellence for Transformative Meta-Optical Systems (TMOS)
University of Technology Sydney
Ultimo, New South Wales 2007, Australia
J. Hruby
Institute for Materials Research (IMO)
Hasselt University
Wetenschapspark 1, Diepenbeek B-3590, Belgium
J. Hruby
IMOMEC Division
IMEC, Wetenschapspark 1, Diepenbeek B-3590, Belgium
F. Jelezko
Centre for Integrated Quantum Science and Technology (IQST)
Ulm University
89081 Ulm, Germany
S. L. Y. Chang
Electron Microscope Unit
Mark Wainwright Analytical Centre
University of New South Wales
Sydney, NSW 2052, Australia

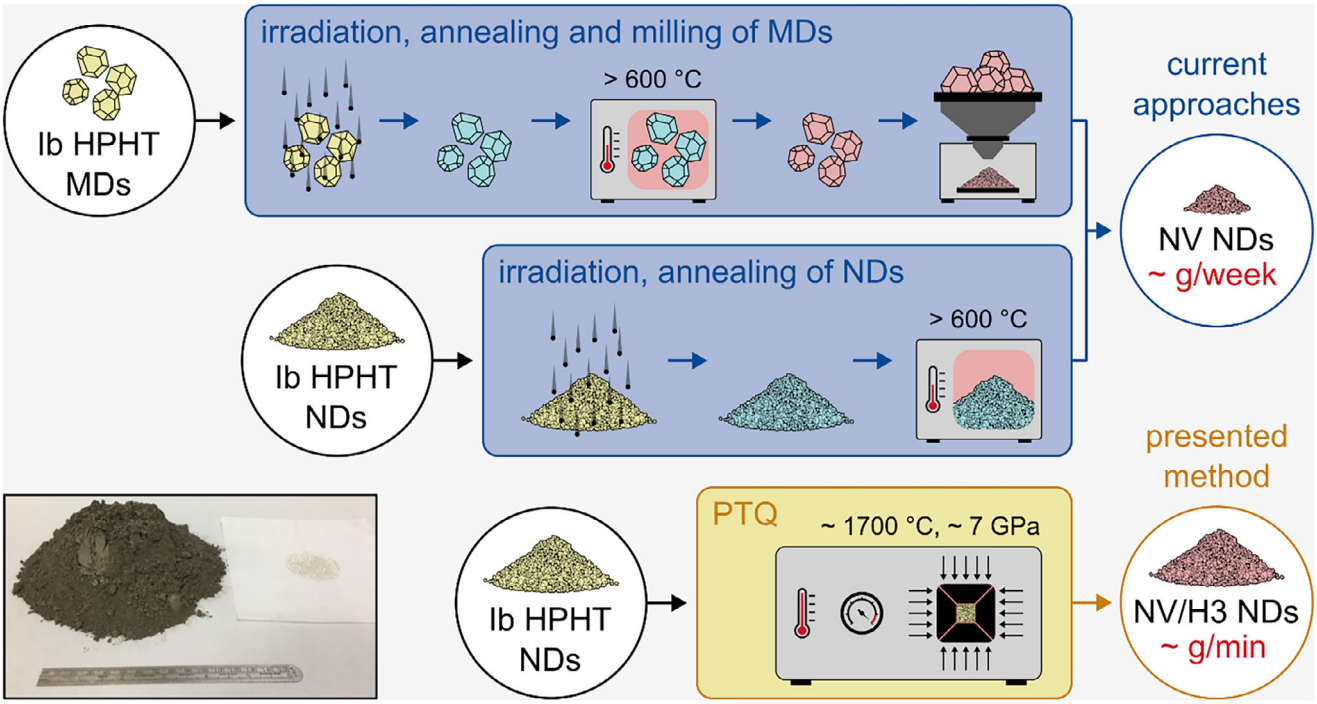

Figure 1. Production of luminescent NDs. The scheme depicts the steps of standardized procedures for irradiation and annealing of nanodiamonds (NDs) or microdiamonds (MDs) to produce NV centers in diamond particles (top two rows) and our pressure & temperature qubits (PTQ) method for NV and H3 creation. Note that PTQ is a single-step process with yields greatly surpassing those of current approaches. The inset shows a photograph of untreated Starting NDs (dark powder) that can be PTQ processed per press in a single workday (1250 carats, or 250 g) and the PTQ oxidized NDs (white powder) that can be produced in a single press run (22.5 carats, or 4.5 g). A 15-cm ruler is shown for scale.

contact, much higher pressures (p_C) exist with $p_C >> p_A > p_{NC}$ capable of inducing plastic deformation in diamond particles at temperatures greater than 730 °C[37] (Figure 2b). After sodium chloride melts at temperatures > 1500 °C, it can operate as a hydraulic fluid, keeping the NDs entirely within the diamond thermally stable region (Figure 2c) and fully suppressing graphite formation.[39]

2.2. PL Measurements Highlight the Enhanced Structural Purity and Charge Stability of PTQ NDs

Next, we compared the PTQ-produced NDs (denoted **"PTQ"**) with luminescent NDs of the same nominal size obtained by the standard electron irradiation and annealing technique (denoted **"COMM"**). We choose these NDs as a benchmark because electron irradiated NDs are commonly used by multiple labs and are also commercially available. Comparably to COMM sample, the PTQ NDs were acid-oxidized, which is a common surface cleaning used for quantum sensing. We also included an air-oxidized sample from the same batch (denoted **"PTQ air"**) and starting non-luminescent ND material before PTQ treatment (denoted **"Starting"**) for comparison. See Methods and Supplementary Information for more details.

Figure 3a,b shows normalized PL spectra measured from a thin ND layer with 532 and 355 nm laser excitation to characterize the NV and H3 centers, respectively. Unlike the Starting material (Figure S4a, Supporting Information), both COMM and PTQ samples clearly show the presence of neutral (NV^0) and negatively charged (NV^-) nitrogen vacancy centers with zero phonon line emissions at ≈575 and ≈637 nm, respectively. Among the NV charge states, NV^- is widely exploited in quantum applications, as it acts as a room-temperature qubit. Its stabilization is thus highly important. It is evident from the measured spectra that PTQ processing yields NDs with greatly higher fractions of NV^- over NV^0, compared to COMM NDs. Because their surface chemistries are similar and we observed similar stabilization for air-oxidized samples (Figure S4, Supporting Information), and because the P1 concentration is high and comparable for all samples (see **Table 1**), we attribute this mostly to the core material properties and thus to the NV creation method. However, we cannot completely exclude that the better NV^- charge stability in PTQ samples is partially due to lower NV concentration (see Table 1). When excited with a 355 nm laser, PTQ NDs exhibit green emission with a major peak ≈520 nm, which we assign to the phonon side band of the H3 center. Some contribution of the NV^0 is also visible. In comparison, COMM NDs show predominantly NV^0 emission, and green PL is nearly absent. Formation of H3 centers in micro-sized diamonds has recently been achieved using HTA with temperatures above 1600 °C; however, graphitization renders HTA treatment in NDs challenging.[30]

The enhanced NV^- stability of PTQ NDs is also preserved at the single-particle level, as is evident from spectral measurements of individual NDs (Figure 3c,d). To quantify the NV^-/NV^0 PL ratio, we deconvoluted each single-particle

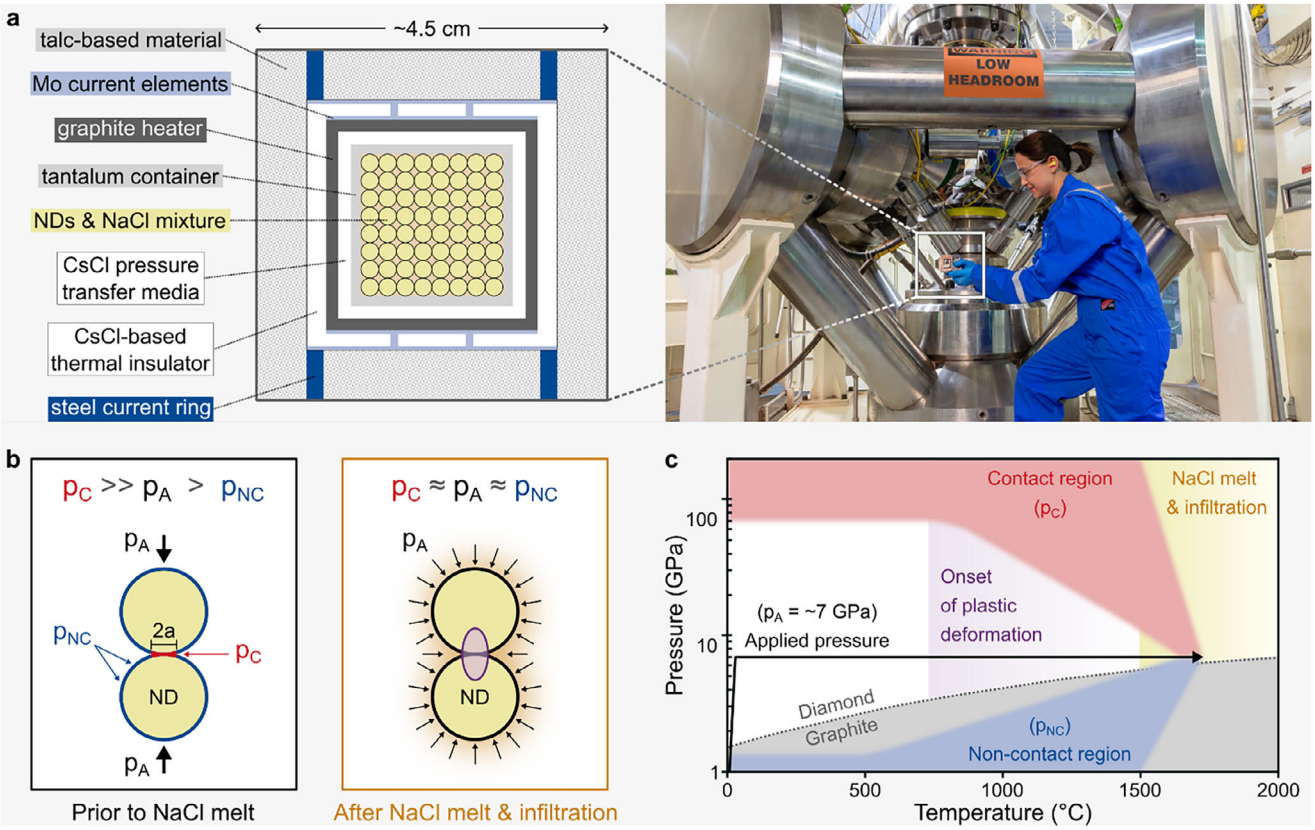

Figure 2. PTQ method. a), The photograph on the right shows a sintering press with a cube-shaped press cell used to encapsulate the ND sample. The schematic on the left depicts the unique cell design, which has been patented and is further described elsewhere.[41,42] b), Schematics illustrating a simplified model of pressures acting upon the NDs in the press cell during PTQ processing prior to and after the sodium chloride melt and infiltration. p_A is the pressure applied to the press cell; p_C and p_{NC} are calculated pressures acting on the NDs at contact or non-contact regions, respectively. The ND parts highlighted in purple indicate the plastically affected region. c), Carbon phase diagram applicable to the PTQ process, showing that it allows for the formation of the NV centers entirely within the diamond-stable region.

spectrum (N = 33) into two fractions, corresponding to NV^- and NV^0, using nonnegative matrix factorization in MATLAB, as previously described[26] (see Supplementary Information). We then integrated the resulting NV^- and NV^0 spectra and calculated the NV^-/NV^0 PL ratio for each single particle. The average NV^-/NV^0 PL ratio from all NDs in the PTQ sample (3.21) was more than two-fold higher than that of the COMM NDs (1.47). For thin-layer measurements, the NV^-/NV^0 PL ratios were generally much higher (5.37 for PTQ and 2.57 for COMM), presumably due to less interaction between the ND surface and the environment. These results are NV-weighted and not ND-weighted, meaning the resulting average values are based on total PL and not on the number of particles, as is the case for individual-ND measurements. Nonetheless, the PTQ sample exhibited a ≈2-fold higher NV^-/NV^0 PL ratio. We note that the exceptional NV^- stability of the PTQ NDs is offset by a lower overall NV PL intensity. In addition, the NV^- $m_s = 0$ and NV^0 excited state lifetimes were measured at a single-particle level. The PTQ sample exhibited a longer NV^- amplitude-averaged lifetime (24.0 ns compared to 19.5 ns for the COMM sample; see Figure 3e) and a smaller contribution from non-radiative pathways (see Supplementary Information), indicative of the superior structural purity and charge stability of PTQ NDs.

2.3. PTQ NDs Display Exceptionally High Rabi Contrast and High Sensitivity for Relaxometry Sensing

To evaluate the impact of the high-temperature plastic deformation on the performance of the NV spin properties, we characterized the samples using optically detected magnetic resonance (**ODMR**) methods at the single-particle level. Fitting of the ODMR spectra revealed that the PTQ sample had a ≈16% smaller splitting of the zero-field NV resonance lines (2*E parameter). This suggests lower internal strain and possibly a lower concentration of charged defects (**Figure** 4a,b), which could be explained by the absence of irradiation-induced defects and high-temperature lattice healing. We then characterized the NDs using Rabi measurements. For this and subsequent quantum studies (excluding all-optical relaxometry), the NV resonances were split using a small static magnetic field of ≈30–60 Gauss. Strikingly, the Rabi contrast of the PTQ sample was ≈5 times higher than that of the COMM sample (Figure 4c,d). Reaching such high contrast (more than 15% on average) in such small ND particles is exceptional, particularly considering that we used a simple single-frequency microwave (**MW**) π pulse (i.e., without applying a chirp or shaped pulses). One of the PTQ NDs even exhibited 40% Rabi contrast (Figure S2 for the measured Rabi curve, Supporting

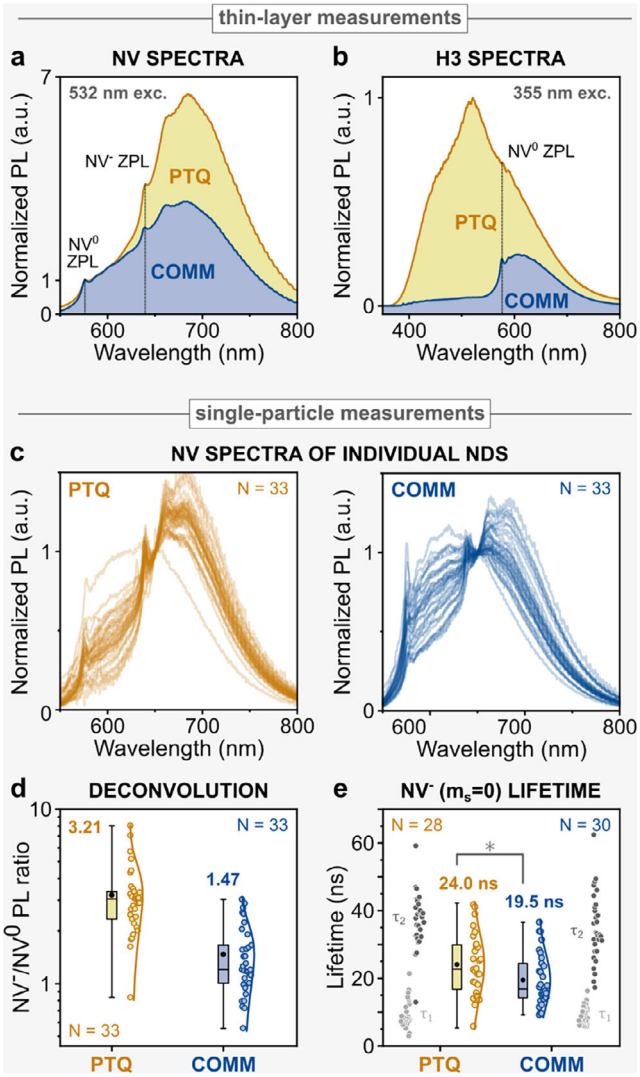

Figure 3. Optical characterization of PTQ NDs. a,b), Spectral measurements from thin ND layers were carried out using 532 and 355 nm laser excitation to detect NV- and H3-related PL, respectively. The vertical dashed lines indicate the NV^- and NV^0 zero-phonon lines (ZPLs). The NV^-/NV^0 PL ratios for the thin-layer measurements were 5.37 for PTQ and 2.57 for COMM. c–e), For single-particle measurements, we used 532 nm laser excitation. c), PL spectra measured from individual NDs normalized to the signal at 650 nm. We chose this point because it lies approximately in the middle of the NV^- and NV^0 PL maxima, thus emphasizing the NV^-/NV^0 ratio. d) NV^-/NV^0 PL ratios calculated from the spectra of individual NDs deconvoluted to NV^- and NV° fractions, see Supplementary Information. e), Fluorescence decay curves of the NV^- excited states. The NV spins were first initialized to $m_s = 0$ using a continuous wave polarization pulse; consequently, a picosecond pulse was used to measure the lifetime. The signal was spectrally filtered by a 760–824 nm band-pass and fitted using a bi-exponential fit. The box plot shows the fit results of individual-particle measurements, where τ_1 values (light grey) are the fast decay contributions, τ_2 values (dark grey) are the slow decay contributions, and yellow/blue points are the amplitude-averaged lifetimes (τ_{AVG}). Statistical analysis of the amplitude-averaged lifetimes indicated a significant difference (Mann-Whitney test; shown as $*$ for $P < 0.05$). We also simultaneously measured the NV^0 lifetime using a 555–595 nm spectral window, see Supplementary Information.

Information), drastically reducing the measurement time needed to obtain a reasonable signal-to-noise ratio. The contrast improvement can be attributed to the enhanced NV^-/NV^0 ratio of the PTQ sample, which would reduce noise in a Rabi measurement from NV^0 and ensure better charge state preparation;[45] the 23% increase in the excited state lifetime of NV^-, which would increase the level of spin polarization in the ground state; and the lower lattice strain.

As quantum sensing sensitivity scales with $1/\sqrt{T_x}$[46], where T_x is the spin relaxation time, NDs must have long T_1 and T_2 times to be suitable for spin-related quantum sensing applications. We therefore performed all-optical (i.e., without MW excitation) and alternating T_1 measurements, both probing the NV spin relaxation from the $m_s = 0$ sublevel, for comparison (Figure 4e,f). We minimized the NV ionization and recombination processes influencing the T_1 measurements[47] by using very low laser power (diminishing laser-induced charge effects)[48] and by only considering particles that did not show obvious charge-related decays.[17] For the PTQ sample, we observed a ≈5-fold longer alternating T_1 time, reaching ≈1 ms bulk-like value. Although alternating relaxometry is less prone to charge influence, we cannot rule it out completely. Compared to COMM NDs, PTQ NDs offer more than double the sensitivity for relaxometry sensing. As the surface treatment and P1 concentration (see below) are similar for both samples, we attribute this improvement to the PTQ technique. We also note that the alternating relaxometry was carried out in the static magnetic field and thus the difference in T_1 times arising from increased NV cross-relaxation due to high NV concentration occurring at near-zero fields[49] should be suppressed in this case. We also measured T_2 time using spin echo and dynamical coupling (XY8) sequences, obtaining comparable results for both samples (Figure 4g,h) as in both cases the decoherence is dominated by the high nitrogen concentration.[50]

2.4. PTQ NDs Display Promising Physicochemical Properties and are Suitable for Biological Applications

We found that the harsh PTQ conditions (1700 °C and 7 GPa) do not introduce diamond sintering, lattice damages, or surface graphitization. Moreover, they lower the lattice strain, resulting in good optical and spin properties. Bright field TEM analysis (**Figure 5**a; Figures S14 and S15, Supporting Information) revealed similar size and shape distributions for PTQ and COMM NDs. Both samples exhibited elongated, irregular shapes, with high aspect ratios (1–2.5) and relatively low circularity and eccentricity (0.4–0.8). Comparing the PTQ sample with the Starting NDs, we observed good overall similarity, demonstrating that the addition of sodium chloride indeed prevents sintering and largely preserves the sizes and shapes. X-ray diffraction (Figure 5d) confirmed that PTQ NDs have a crystalline cubic diamond structure, without formation of mixed hcp and cubic phases as suggested in other work.[51] Moreover, based on Raman spectroscopy (Figure 5e), the structure appears highly crystalline with very little introduction of surface graphitization. This is further corroborated by high-resolution TEM images and the corresponding lattice strain maps (Figures 5b,c), showing no apparent structural faults or lattice strains. These findings agree well with the ODMR

Table 1. Overview of material and optical properties of ND samples. N.A. stands for not available, and N.M. for not measured. The errors are given as standard deviations (Zeta, TEM), standard errors (optical measurements), or are further described in Supplementary Information (EPR, NMR). ZFS stands for zero-field splitting. "Avg. PL" is the average photoluminescence measured from individual NDs using objective with 1.5 numerical aperture and 44 μW 532 nm laser. See Supplementary Information for more details on the measured values.

	PTQ conditions	Surface treatment	Zeta potential (mV)	TEM			NV optical measurements											EPR and NMR			
				Size (nm)	Aspect ratio	Circularity	Avg. PL (kcts./s)	NV^-/NV^0 PL		Lifetime (ns)		ZFS 2*E (MHz)	Contrast Rabi (%)	T_1 (μs)		T_2 (μs)		P1 conc. (ppm)	NV conc. (ppm)	NV T_2 time (μs)	^{13}C T_1 time (s)
								Single	Thin layer	NV^- (m_s=0)	NV^0			All-optic.	Alternating	Spin echo	XY8				
Starting	N.A.	N.A.	-38 ± 3	43.3 ± 17.4	1.54 ± 0.43	0.59 ± 0.13	N.A.	N.A.	N.A.	N.A.	N.A.	N.A.	N.A.	N.A.	N.A.	N.A.	N.A.	9.6 ± 1.9	<0.05	N.A.	64 ± 12
PTQ	1700 °C 7 GPa 4 min	acid ox.	-45 ± 2	52.0 ± 14.5	1.41 ± 0.34	0.70 ± 0.13	151 ± 19	**3.21 ± 0.26**	**5.37**	**24.0 ± 1.7**	**41.6 ± 2.7**	**15.2 ± 1.0**	**15.9 ± 1.8**	**244 ± 35**	**989 ± 172**	1.23 ± 0.10	4.38 ± 0.53	10.9 ± 2.1	0.31 ± 0.02	0.72 ± 0.04	**55 ± 15**
PTQ air	1700 °C 7 GPa 4 min	air ox.	-41 ± 4	45.4 ± 13.4	1.58 ± 0.46	0.58 ± 0.15	152 ± 16	2.02 ± 0.18	4.03	N.M.	N.M.	N.M.	N.M.	170 ± 21	N.M.	N.M.	N.M.	9.7 ± 1.9	0.44 ± 0.03	0.66 ± 0.04	4 ± 1
COMM	N.A.	acid ox.	-32 ± 3	47.5 ± 17.6	1.55 ± 0.47	0.62 ± 0.15	**872 ± 157**	1.47 ± 0.12	2.57	19.5 ± 1.4	31.6 ± 2.0	18.2 ± 1.3	3.2 ± 0.3	170 ± 16	208 ± 40	1.14 ± 0.08	5.45 ± 0.81	8.6 ± 1.7	**2.94 ± 0.18**	**1.28 ± 0.03**	22 ± 5

results and provide further support that the PTQ process yields a high degree of lattice crystallinity, resulting in excellent NV spin properties.

Surface structures and chemistry of NDs are other important factors in stabilizing NVs. C 1s XPS spectra indicated that PTQ NDs have higher sp^3 and negligible sp^2 content (93.0% and 0.2%, respectively) compared to COMM NDs (87.0% and 4.7%, respectively) and Starting samples (86.0% and 5.6%, respectively) (see Figure 5f; Table S2 and Figure S8, Supporting Information). Additionally, the zeta potential of the PTQ sample was lower than that of the COMM NDs (see Table 1), suggesting a higher level of oxidation, which could partly explain the better NV^- stability. The oxidized surfaces of PTQ NDs were also observed using Fourier-transform infrared spectroscopy (FTIR), shown in Figure 5g and further discussed in Supplementary Information).

Furthermore, we characterized the samples by spin-counting with electron paramagnetic resonance (**EPR**) in the X-band (≈8–10 GHz) (see Table 1 and Supporting information). The P1 concentration (≈10 ppm) was rather homogeneous across samples and expected for this size range of NDs (see Supplementary Information). The NV concentration was lower in the PTQ sample, which agrees well with PL measurements of individual NDs. Nonetheless, the brightness was sufficient for single-particle quantum-sensing experiments, and further optimization of PTQ conditions is feasible to increase the NV conversion efficiency. As expected, the NV center signal was not detected in the Starting sample, indicating that the NV concentration is below the EPR detection limit of ≈0.05 ppm and that the PTQ treatment yields NV centers. Additionally, we studied NV coherence times (T_2) using pulsed EPR (see Table 1). Unlike the results of optical measurements, the COMM material showed longer coherence compared to the PTQ NDs (1.28 and 0.72 μs, respectively). This discrepancy could be partially explained by the fact that only optically active NVs are probed with optical methods.

Nuclear magnetic resonance (**NMR**) acquisitions were used to determine the ^{13}C spin-lattice relaxation time (T_1), which is an important parameter in the context of nuclear hyperpolarization experiments.[52,53] The ^{13}C T_1 in the PTQ sample was close to that of the Starting material (T_1 ≈ 55 and 64 s, respectively), demonstrating that the PTQ process is efficient in terms of preserving the ^{13}C T_1. For comparison, the COMM material exhibited faster ^{13}C T_1 relaxation (T_1 ≈ 22 s). This could be explained by the irradiation-induced generation of lattice defects (such as vacancy clusters),[54] but also by the presence of surface impurities (see Supplementary Information).

Lastly, as many ND quantum sensing applications aim to probe biological environments, we studied whether the PTQ material maintains the non-cytotoxic properties typical of NDs and can be visualized inside cells. Extensive cytotoxicity analysis, involving four human cancer lines varying in tissue origin, proliferation, and metabolic activity, as well as normal human somatic cells, indicated the clear absence of cytotoxicity (Figure 5h). Furthermore, we found that both H3 and NV fluorescence in HeLa cells can be detected using a standard commercial confocal microscope (Figure 5i). The H3 and NV signals were highly correlated (Pearson's Coefficient r > 0.94) (see Supplementary Information for more information). This is, to our knowledge, the first H3 imaging in a cellular environment using such small NDs.

3. Discussion

We describe a single-step, cost-effective method that yields ≈250 grams of ≈50-nm luminescent NDs per workday from non-luminescent material using a commercial sintering press apparatus modified for ND processing. Our results indicate that the

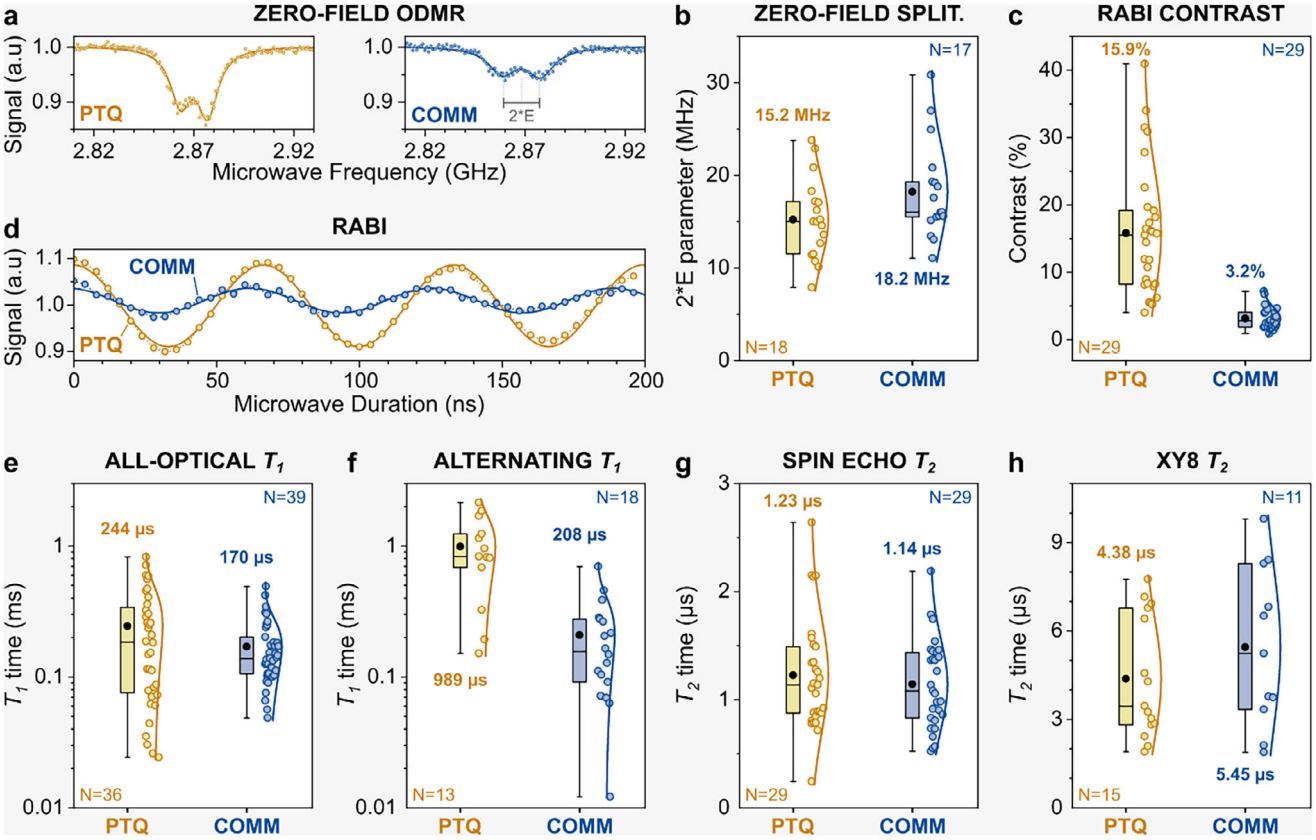

Figure 4. Quantum properties of PTQ NDs measured at the single-particle level. a), Zero-field ODMR measurements showing characteristic spectra of individual PTQ and COMM ND particles. The datapoints (dots) are fitted with a double Lorentzian function (solid lines). b), Box plot showing 2*E splitting parameters obtained from the fits of the zero-field ODMR spectra. c), Box plot showing Rabi contrast obtained from the fits of the Rabi measurements. d), Rabi measurements showing characteristic oscillations obtained from individual PTQ and COMM ND particles. The datapoints (dots) are fitted with sine curve (solid line). e–h), Box plots showing results of time constants obtained by single-exponential fits of single-particle measurements using e) all-optical T_1, f) alternating T_1, g) spin echo T_2, and h) XY8 T_2 sequences.

high-temperature plastic deformation not only preserves the diamond crystallinity and prevents graphitization, but also induces lattice healing manifested in lesser lattice strain and prolonged NV and ^{13}C T_1 spin relaxation compared to standard methods of NV production. One of our most striking findings is the ≈5 times higher Rabi contrast, which we attribute in part to the greater than two-fold higher NV^-/NV^0 ratio and 23% longer excited state lifetime of the NV^- $m_s = 0$ sublevel. We thus conclude that these NDs are highly suitable for quantum applications, in which spin contrast, spin relaxation, and NV^- stability are paramount. Additionally, PTQ's capability of producing diamagnetic H3 centers, even in small NDs, opens new avenues for multifunctional imaging.

The demonstrated NV yield of PTQ processing is, however, lower in comparison to the standard irradiation/annealing methods. Future work, including optimizing the processing conditions by separating the contributions of various temperature and pressure levels on NV yield, can be carried out for applications requiring maximum ND brightness. While the conditions used here (1700 °C, 7 GPa, 4 min) represent a balanced selection that simultaneously promotes formation of both NV and H3 centers and yields high-quality NVs, preliminary results indicate that higher temperatures generally favor H3 center formation, consistent with previously published findings,[30] while lower temperatures favor NV creation until a threshold is reached.

Overall, our high-yield production method enables abundant use of fluorescent NDs without concerns over resource consumption, holding significant potential to drive their broader commercial adoption across various industries.

4. Experimental Section

PTQ Method for Fluorescent ND Production: The PTQ NDs were fabricated from commercially available non-luminescent 50-nm diamond powder (denoted as **Starting**) milled from diamonds containing ≈120 ppm substitutional nitrogen (grade MA4, Engis Corporation, Wheeling, Illinois). The diamond powder was mechanically blended with sodium chloride in a ratio of 75/25 wt.% by ball milling in isopropanol. The ND/NaCl mixture was loaded into a Ta metal container and then into a cubic press cell.[41,42] It was subjected to PTQ treatment at 7 GPa and 1700 °C for 4 min in a cubic-type press[43] manufactured by MegaDiamond. The press cell contained an internal circuit with a resistive heating element, allowing simultaneous pressurization and heating.[41,43] The PTQ-treated NDs were washed with deionized water to remove sodium chloride and then sonicated in an ultrasonic bath to break down the agglomerates. The NDs were then either air oxidized at 475–500 °C (denoted as **PTQ air**) or acid

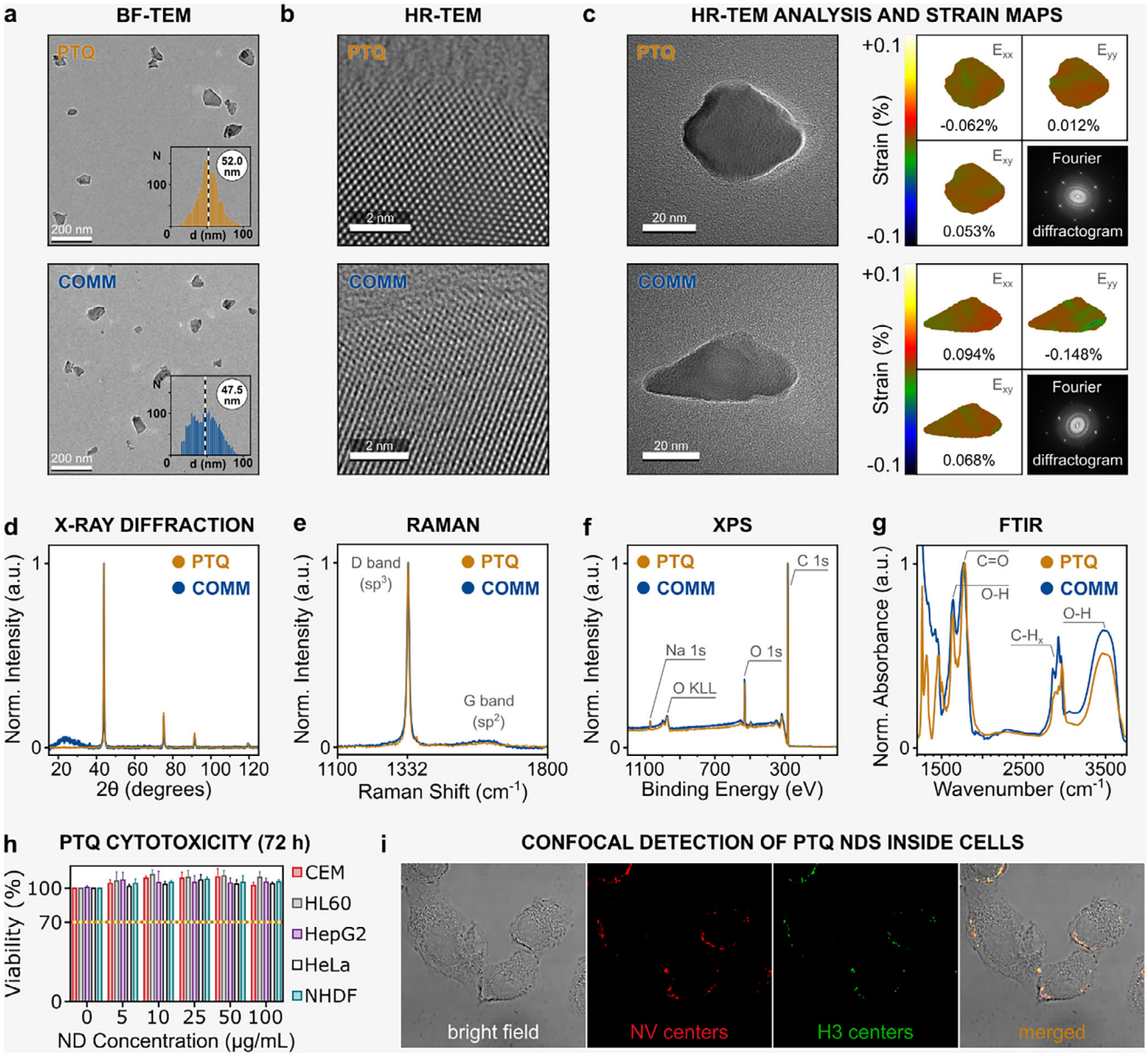

Figure 5. Material and other properties of ND samples. a), Representative bright field (BF) TEM images of ND samples. The insets show the TEM-calculated histograms of particle diameters analyzed from more than 2500 individual NDs (see Figure S14, Supporting Information). The resulting average equivalent diameter for each sample is given in the white circle and is visualized as a vertical dashed line. b), High-resolution (HR) TEM images showing ND surface structures. c), HR-TEM images of individual NDs and their corresponding strain field maps of E_{xx}, E_{yy}, and E_{xy} tensors based on the {111} and {200} reflections and Fourier diffractograms showing the diamond lattice structures. The average strain within the particle is indicated in the image. d), X-ray powder diffractogram. Peaks at 2θ value of 43.90, 75.21, 91.5, and 119.5 represent {111}, {220}, {311}, and {400} crystallographic planes, respectively. e), Raman spectrum normalized to the diamond Raman peak at 1332 cm^{-1}. The broad G band at 1583 cm^{-1} originates from sp^2-hybridized carbon atoms. The structure of NDs is highly crystalline with very little introduction of surface sp^2 defects, evidenced by the very low G band. f), XPS spectra normalized to the C 1s peak. For a description of spectral analysis and deconvolution of C 1s and O 1s peaks, please refer to the Supplementary Information. g), FTIR spectra normalized to the C═O band. The PTQ and COMM spectra are similar and characteristic for the oxidized ND surface. h), Cell viability in the presence of PTQ NDs incubated for 72 h with increasing ND concentrations. Cell viability was assessed using the CellTiter-Glo® 2.0 assay. The cytotoxicity threshold (yellow dotted line) is indicated at 70% viability (ISO 10993–5:2009). Data are presented as the mean values from quadruplicate samples. Results were normalized to the control cells (without PTQ treatment). Error bars represent standard deviations. Additional cytotoxicity test results using PTQ NDs prepared from a stock solution in 1.5% BSA (not shown) and for 24-h incubation (not shown) were similar – no cytotoxicity was detected. i), Confocal section from HeLa cells transfected with PTQ NDs. The H3 centers (excited with a 440 nm laser) are shown in green, and NV centers (excited with a 561 nm laser) are shown in red. Areas of colocalization appear yellow in the merged BF image.

oxidized using concentrated sulfuric and nitric acid (3:1 ratio) heated to 90 °C for 10 h, and washed (denoted as **PTQ**).

Commercial Fluorescent NDs: As a commercially available comparison, we used NDNV50nmHi 50 nm NDs from Adamas Nanotechnologies, Inc. (denoted as **COMM**). These NDs are presumably acid oxidized, as they contain carboxyl surface groups.

Particle Dynamic Light Scattering (DLS) Measurements: To measure the hydrodynamic radius and zeta potential of NDs in aqueous solutions, we used a Zetasizer Nano instrument (Malvern Panalytical) and disposable folded capillary cells (DTS1070). The ND concentration in MilliQ water was 0.1 mg/mL without any salt added (for DLS) or with 1 mM NaCl to provide sufficient conductivity (for zeta potential). Measurements were made in triplicates and averaged.

PL and Raman Characterizations: For the luminescence (Figure 3) and Raman (Figure 5) spectral measurements, we used a commercial WITec alpha300R confocal Raman microscope. A thin layer of NDs was deposited by drop casting of the ND aqueous solution (3 µl droplet of 1 mg mL^{-1}) on silicone substrate followed by evaporation at elevated temperatures (55 °C) – repeated 12 times. The NV luminescence spectra were acquired for 20 s at 8 random spots using a 10X ZEISS EC Epiplan objective (N.A. = 0.25) and a 532 nm laser with a power of 200 µW (measured before objective) and averaged. The H3 luminescence spectra were acquired for 40 s at 5 random spots using a Thorlabs LMU-40X-NUV MicroSpot Objective (N.A. = 0.47) and a 355 nm laser with a power of 1 mW (measured before objective) and averaged. Spectra were detected using an Andor CCD camera coupled with a WITec UHTS300 spectrometer (150 lines mm^{-1} grating blazed for 500 nm). Raman spectra were acquired for 50 s at 8 random spots using a Thorlabs LMU-40X-NUV MicroSpot Objective (NA = 0.47) and a 355 nm laser with a power of 1 mW (measured before the objective) and averaged. Raman signals were detected using an Andor CCD camera coupled with a WITec UHTS400 spectrometer (1200 lines mm^{-1} grating blazed for 300 nm).

For single-particle measurements, the cover glasses were cleaned in a sonication bath using tetrahydrofuran, ethanol, methanol, and MilliQ water (in that order); dried; and cleaned for 30 min in UV Ozone Cleaner (BioForce ProCleaner). The NDs were deposited on the cover glass using a vacuum-free Ossila Spin Coater (dynamic spin coating of 10 µl of 10 µg ml^{-1} aqueous ND solution at 1000 rpm). The single ND photoluminescence was excited by focusing a 532 nm laser of 40 µW power (measured before the objective) trough oil objective (Olympus UPLAPO100XOHR, N.A. = 1.5). Signals were collected using the same objective and detected using an Andor CCD camera coupled with a WITec UHTS300 spectrometer (150 lines mm^{-1} grating blazed for 500 nm). The total integration time varied based on the signal intensity to reach a sufficient signal-to-noise ratio. The XYZ position of the piezo stage was optimized before each measurement so that the beam was in the middle of the particle using automatic position optimization controlled by a custom-written LabView program. The NV spectral deconvolution was carried out using nonnegative matrix factorization in MATLAB (see Supplementary Information).

Lifetime Measurements: For lifetime measurements (Figure 3), samples were prepared by drop casting an ND solution onto the surface of plasma-cleaned glass slides. Isolated single NDs were prepared using low ND concentrations of ≈1 µg mL^{-1}. The samples were mounted in a home-built confocal microscope setup, and the Qudi software package was used to locate individual NDs. The samples were illuminated using a continuous wave, 532 nm GEM laser modulated using an AOM for NV^- spin polarization, as well as a PicoQuant 532 nm pulsed laser with a variable repetition rate. The fluorescence from the NDs was captured using two single-photon counting avalanche photodiodes (APDs), which were filtered at different spectral regions corresponding to the NV^- (792/64 nm band-pass) and NV^0 (575/40 nm band-pass) charge states. The TTL pulses from the APDs were fed into separate inputs of an ID-Quantique ID1000 fast-counting card. This allowed the lifetimes of the NV^- and NV^0 excited states to be measured independently.

The lifetime measurement sequence (Figure S5), Supporting Information began with a 3 µs initialization pulse (30 µW) using the continuous wave GEM laser. This was followed by a 1 µs waiting time, which allowed the system to relax to the ground state. If the NV^- charge state has been successfully initialized, there is an 85% chance of the $m_s = 0$ spin state being occupied. This imperfect initialization process leads to fluorescence being observed from both NV^- spin states, as well as from the NV^0 charge state. Following the 1 µs waiting period, a picosecond pulse from the 532 nm PicoQuant laser drives a single-photon process that excites the system from the ground state to the excited state of either the NV^- or NV^0 state, depending on the result of the initialization. This pulse triggers the fast-counting card to begin recording for 600 ns. The fluorescence resulting from any subsequent radiative transitions was measured using the two APDs. Histograms for each charge state were populated by repeating this measurement many times.

Optical Quantum Measurements: For optical quantum measurements (Figure 4), samples were prepared by drop casting an ND solution onto the surface of plasma-cleaned glass slides. Isolated single NDs were prepared using low ND concentrations of ≈1 µg mL^{-1}. To apply the MW field, the ND-coated cover glasses were mounted on a custom-made printed circuit board (PCB), and a 20 µm thick copper wire was stretched over the sample and soldered onto the PCB. The all-optical T_1 relaxometry of individual ND particles was performed using a commercial WITec alpha300R confocal Raman microscope (**setup 1**) modified to enable pulse laser excitation and time-resolved single photon detection. The rest of the measurements were carried out using a custom-built confocal fluorescence microscope (**setup 2**). In both cases, a 532-nm laser was used to excite the NV centers. The laser was focused onto the sample using an oil-immersion objective (Olympus UPLAPO100XOHR 100× oil, N.A. = 1.5 for setup 1 and Olympus UPlanSApo 60× oil, N.A. = 1.35 for setup 2). The laser power measured before the objective was 44 µW (setup 1) or 70 µW (setup 2). The NV fluorescence was collected using the same objective, filtered through a 650-nm longpass filter, and detected with a single-photon counting avalanche photodiode. The T_1 and T_2 data were fitted with monoexponential decay functions to obtain spin relaxation and coherence times, respectively. The Rabi, T_1, and T_2 measurements on setup 2 were performed in a magnetic field of ∼30–60 Gauss. The quantum measurements were performed using custom-written LabView (setup 1) and Qudi (setup 2) software. More details are in Supplementary Information.

Transmission Electron Microscopy and Particle Size and Shape Analysis: Bright field TEM images for size analysis were performed with a JEOL2100Plus electron microscope operated at 200 kV. The rest of the BF and high-resolution (HR) TEM images were performed with a JEOL F200 cold field emission electron microscope operated at 200 kV equipped with a Gatan Oneview camera. TEM samples were prepared on commercial copper grids (SPI 300 mesh regular grid), which we coated with parloidon and subsequently with carbon membrane for better dispersion. First, the grids were placed on a droplet (20 µl) of poly(ethyleneimine) solution (M_W = 2.5 kDa, 0.1 mg mL^{-1}). After incubation (2 min for Starting and PTQ air and 10 min for PTQ and COMM), the solution was gently removed using a tissue, and the grids were placed on a droplet of water (20 µl). After 1 min, the solution was again removed with a tissue. Then, the grids were placed on a droplet (20 µl) of aqueous ND solution (0.05 or 0.1 mg mL^{-1}) and incubated for 10 min. Finally, residues were removed with a tissue, and the grids were left to dry for 30 min in a Petri dish. Ultrathin carbon TEM grids with copper meshes were used for HR-TEM imaging for lower background contrast. Particle size analysis was conducted using an in-house MATLAB code. Particle shape analysis was conducted using an in-house Python program. The strain field analysis of the nanodiamond particles was carried out from the HR-TEM images of NDs, using the Geometric Phase Analysis (GPA) implemented on GMS software (Gatan Inc.). {111} and {002} reflections from the Fourier diffractograms of the HR-TEM image were selected to calculate the displacement fields. From the displacement fields, local strains were then calculated to form strain maps. The reference diamond lattice was selected from a 5×5 nm^2 region within the particle. See Supplementary Information for more details.

FTIR Measurements: FTIR spectra for all samples were measured using a Perkin FTIR Spectrum 100 spectrometer. Transmittance of each sample was analyzed in powder form by placing 20 mg of the sample on a diamond ATR crystal with a scan rate of 16 Hz. Prior to measurement of each sample, the ATR crystal was cleaned with ethanol and a background

measurement was taken. All analyses were conducted with 128 scans collected over the region of 4000–500 cm^{-1}

Powder X-Ray Diffraction Measurement: Powder X-ray diffraction (XRD) measurements were performed using a PANalytical Xpert Multipurpose XRD system (MPD) equipped with a Cu-Kα radiation source (theta to theta goniometer system, curved monochromator). Dried powder samples (10 mg) were placed on a glass substrate pre-cleaned with acetone and deionized water. Intensities corresponding to scattering angles were measured from 10 degrees (2 theta) to 125 degrees (2 theta) to consider all four major peaks of the NDs.

X-Ray Photoelectron Spectroscopy (XPS) Measurement: XPS was performed using Thermo Fisher Scientific's ESCALAB250Xi instrument equipped with monochromated Al K alpha (energy 1486.68 eV) operated at room temperature with 120 W power, 90 degrees photoelectron take off angle (electron optics respect to surface plane), 100 eV pass energy for surface scan, 20 eV pass energy for region scans, and a spot size of 500 micrometers. Spectra were analyzed with Avantage software. The binding energy reference was considered to be 284 eV (C 1s) for nanodiamond.

Solid-State EPR and NMR: A Bruker Elexsys E580 spectrometer operating in the X-band frequency range (9–10 GHz) was used to perform EPR characterization of the samples. P1 and NV spin densities were estimated using continuous wave EPR with an ER-4122-SHQE resonator of typical quality factor $Q = 8000–10000$. NV coherence times were measured using an ER-4118X-MD5 pulsed FlexLine resonator. NV spectra simulations were performed using the EasySpin software package in Matlab. NMR experiments were performed using a 300 MHz wide-bore (WB) system at a magnetic field strength of B = 7.05 T combined with an Avance III console, both provided by Bruker Biospin GmbH. At this magnetic field, the corresponding Larmor frequency for ^{13}C nuclei is $f(^{13}C) = 75.513$ MHz.

Assessment of PTQ Toxicity: The cytotoxicity of PTQ NDs was evaluated in four cancerous cell lines (CEM, HL-60, HepG2, HeLa) and normal human dermal fibroblasts (NHDF). All cell lines were obtained from ATCC (Manassas, VA, USA) and tested negative for the presence of Mycoplasma (MycoAlert Mycoplasma Detection kit, Lonza). The cells were cultured in DMEM high-glucose medium containing 10% FBS and 1% GlutaMax. Cells were seeded into 384-well white plates (Thermo Fisher Scientific, Waltham, USA) at concentrations of 3000, 4000, 800, 600, and 1000 cells per well, respectively, and left to rest overnight. PTQ was prepared at a stock concentration of 5 mg mL^{-1} in either water or 1.5% bovine serum albumin to ensure particle stabilization in the media. The cells were treated with PTQ at final concentrations of 0, 5, 10, 25, 50, or 100 µg mL^{-1} and incubated at 37 °C with 5% CO_2 for 24 and 72 h. After the incubation period, cell viability was assessed using the CellTiter-Glo 2.0 detection reagent (Promega). Luminescence was measured using a multimode plate reader (TECAN Spark). The luminescence signals of samples treated with PTQ were compared to the signal of control cells treated with the diluent (water or 1.5% bovine serum albumin) alone, which was set to represent 100% cell viability.

Cell Culture and Fluorescence Microscopy Imaging of NDs: To ensure the stabilization of PTQ under biologically relevant conditions, NDs were pretreated either by polyglycerol (PG) or bovine serum albumin (BSA). For PG coating, 2 mg of NDs were sonicated in glycidol (240 µl) using a cup horn sonicator. The colloidal ND solution in glycidol was then transferred to a pressure tube and heated to 130 °C under continuous stirring for 40 min. After the reaction, the reaction mixture was transferred to two Eppendorf tubes and centrifuged at 30,000 g for 40 min (20 °C) twice with dimethylformamide, once with methanol, and twice with water. BSA was physically adsorbed onto PTQ by mixing a PTQ stock solution in water (10 mg ml^{-1}) with an equal volume of sterile BSA (3% w v^{-1}) in a sonication bath. The mixture was then incubated using a mixer at 500 rpm for 20 min and was either used immediately for cell experiments or stored at 4 °C for later use.

HeLa cells were seeded in DMEM supplemented with 10% FBS (1 mL) on cover slips in 24-well plates at a density of 4×10^4 cells per well. The following day, the cells were treated with polyglycerol-coated PTQ using Turbofect transfection reagent (ThermoFisher Scientific) as follows: 25 µg PTQ were mixed with 2 µl Turbofect in 100 µl of serum-free medium, and the mixture was incubated at room temperature for 20 min. The mixture was then added dropwise to each well. The cells were incubated overnight at 37 °C in 5% CO_2. After 16 h, the cells were washed twice with phosphate-buffered saline (PBS), fixed with 3.7% paraformaldehyde for 15 min at room temperature, and washed four times with PBS and once with MilliQ water. The coverslips were mounted in water using SecureSeal Imaging Spacers (Grace Bio-Labs).

Confocal images of the cells were acquired using an SP8 confocal microscope (Leica, Mannheim, Germany), equipped with an HC PL APO CS2 63x/1.40 oil objective and sensitive single-molecule hybrid detectors (HyD). The H3 centers and NV centers were visualized by excitation with a 440 nm diode laser (Picoquant, Berlin, Germany) in the emission range of 497–552 nm and with a DPSS 561 nm laser in the emission range of 700–800 nm, respectively. Co-localization analysis was performed with the JACoP Plugin in Fiji ImageJ 1.54f.

Supporting Information

Supporting Information is available from the Wiley Online Library or from the author.

Acknowledgements

The authors thank IOCB's Biochemical Pharmacology core facility for the assessment of cytotoxicity of PTQ, namely Helena Mertlíková-Kaiserová and Eva Tloušťová. The authors also thank IOCB's Microscopy Core Facility, namely Petro Khoroshyy and especially Jana Humpolíčková for technical support during confocal microscopy. The authors further thank Philipp Reineck and Giannis Thalassinos (both RMIT University) for providing help with the non-negative matrix factorization method for deconvolution of NV spectra. TEM facilities at the Electron Microscopy Unit (EMU), Mark Wainwright Analytical Centre is acknowledged. S.L.Y.C. acknowledges the funding from the Australian Research Council Industrial Transformation Training Centre for Next Generation Technologies in Biomedical Analysis (IC210100056), and the UNSW Faculty of Science Seed Fund (INSF). J.H. acknowledges the Flanders Innovation & Entrepreneurship (VLAIO) – Innovation mandate HBC.2022.0211. F.J. acknowledges Horizon Europe (HORIZON) via SPINUS, C-QuENS, QCIRCLE, FLORIN, QuMicro, ERC via HyperQ Project, Carl Zeiss Stiftung (IQST, Ultrasens-Vir, QPhoton), BMBF via projects QSENS, DiaQNOS, QUAMOPOLIS, EXTRASENS, BMWK via project Quasimodo, DFG via projects 445243414, 387073854, 491245864, 386028944, and JE 290/44-1. P.C. acknowledges funding by the Czech Academy of Sciences – Strategy AV21 (VP29), Czech Science Foundation project no. 23–04876S, European Union project C-QuENS (grant no. 101135359), Horizon Europe MSCA-SE project FLORIN (grant agreement ID: 101086142), Technology Agency of the Czech Republic, project TH90010001 EXTRASENS (ERA-NET/QuantERA Cofund Project), and by a grant from the Programme Johannes Amos Comenius under the Ministry of Education, Youth and Sports of the Czech Republic CZ.02.01.01/00/22_008/0004558 Advanced Multiscale Materials for Key Enabling Technologies. I.A. acknowledges financial support from the Australian Research Council (CE200100010, FT220100053).

Conflict of Interest

J. D. Belnap and Y. Bao are employees of Megadiamond, a commercial supplier of diamond products for various applications.

Author Contributions

Y.B. and M.G. contributed equally to this work. Y.B. and D.B. developed the PTQ technique and prepared the luminescent NDs; M.G. carried out spectral, Raman, all-optical T_1, and PL imaging measurements, analyzed and visualized the data, and wrote the manuscript; P.K. and S.L.Y.C carried out BF- and HR-TEM, FTIR, XRD, and XPS measurements; J.C. processed

the NDs and carried out BF-TEM, zeta, and DLS measurements; P.B. carried out ODMR and pulsed-ODMR measurements; Y.M. carried out EPR measurements; R.B. carried out NMR measurements; M.O.-F. carried out lifetime measurements; H.W carried out GPA analysis for ND strain mapping; H.S. carried out the biological experiments; H.Z.J.Z., B.W., and I.A. participated in preliminary ND characterization; J.H. developed acquisition software and helped with data processing. All authors discussed the results and contributed to manuscript writing. F.J., D.B., S.L.Y.C., and P.C. supervised the joint efforts.

Materials & Correspondence

J. D. Belnap (nanodiamond production), S. L. Y. Chang (TEM, FTIR, XRD, and XPS data), P. Cigler (all other spectroscopic, ODMR, EPR, and NMR data, zeta potentials, DLS, and cell experiments).

Data Availability Statement

The data that support the findings of this study are openly available in Zenodo at, https://doi.org/10.5281/zenodo.15986430, reference number 15986431.

Keywords

diamond biosensor, fluorescent nanodiamond, HPHT processing, nitrogen-vacancy center, quantum sensing

Received: August 9, 2025
Revised: August 29, 2025
Published online:

[1] N. Aslam, H. Zhou, E. K. Urbach, M. J. Turner, R. L. Walsworth, M. D. Lukin, H. Park, *Nat. Rev. Phys.* **2023**, *5*, 157.
[2] G. Balasubramanian, P. Neumann, D. Twitchen, M. Markham, R. Kolesov, N. Mizuochi, J. Isoya, J. Achard, J. Beck, J. Tissler, V. Jacques, P. R. Hemmer, F. Jelezko, J. Wrachtrup, *Nat. Mater.* **2009**, *8*, 383.
[3] G. Wolfowicz, F. J. Heremans, C. P. Anderson, S. Kanai, H. Seo, A. Gali, G. Galli, D. D. Awschalom, *Nat. Rev. Mater.* **2021**, *6*, 906.
[4] T. Zhang, G. Pramanik, K. Zhang, M. Gulka, L. Wang, J. Jing, F. Xu, Z. Li, Q. Wei, P. Cigler, Z. Chu, *ACS Sens.* **2021**, *6*, 2077.
[5] Y.-R. Chang, H. Y. Lee, K. Chen, C. C. Chang, D. S. Tsai, C. C. Fu, T. S. Lim, Y. K. Tzeng, C.-Y. Fang, C. C. Han, H. C. Chang, W. Fann, *Nat. Nanotechnol.* **2008**, *3*, 284.
[6] Y. Wu, T. Weil, *Adv. Sci.* **2022**, *9*, 2200059.
[7] G. Q. Liu, R. B. Liu, Q. Li, *Acc. Chem. Res.* **2023**, *56*, 95.
[8] G. Petrini, G. Tomagra, E. Bernardi, E. Moreva, P. Traina, A. Marcantoni, F. Picollo, K. Kvaková, P. Cígler, I. P. Degiovanni, V. Carabelli, M. Genovese, *Adv. Sci.* **2022**, *9*, 2202014.
[9] J. Barton, M. Gulka, J. Tarabek, Y. Mindarava, Z. Wang, J. Schimer, H. Raabova, J. Bednar, M. B. Plenio, F. Jelezko, M. Nesladek, P. Cigler, *ACS Nano* **2020**, *14*, 12938.
[10] T. Rendler, J. Neburkova, O. Zemek, J. Kotek, A. Zappe, Z. Chu, P. Cigler, J. Wrachtrup, *Nat. Commun.* **2017**, *8*, 14701.
[11] S. J. Yu, M. W. Kang, H. C. Chang, K. M. Chen, Y. C. Yu, *J. Am. Chem. Soc.* **2005**, *127*, 17604.
[12] V. N. Mochalin, O. Shenderova, D. Ho, Y. Gogotsi, *Nat. Nanotechnol.* **2012**, *7*, 11.
[13] B. S. Miller, L. Bezinge, H. D. Gliddon, D. Huang, G. Dold, E. R. Gray, J. Heaney, P. J. Dobson, E. Nastouli, J. J. L. Morton, R. A. McKendry, *Nature* **2020**, *587*, 588.
[14] H. S. Knowles, D. M. Kara, M. Atatüre, *Nat. Mater.* **2014**, *13*, 21.
[15] G. Kucsko, P. C. Maurer, N. Y. Yao, M. Kubo, H. J. Noh, P. K. Lo, H. Park, M. D. Lukin, *Nature* **2013**, *500*, 54.
[16] L. P. McGuinness, Y. Yan, A. Stacey, D. A. Simpson, L. T. Hall, D. Maclaurin, S. Prawer, P. Mulvaney, J. Wrachtrup, F. Caruso, R. E. Scholten, L. C. L. Hollenberg, *Nat. Nanotechnol.* **2011**, *6*, 358.
[17] M. Gulka, P. Balasubramanian, E. Shagieva, J. Copak, J. Khun, V. Scholtz, F. Jelezko, S. Stehlik, P. Cigler, *Carbon* **2024**, *224*, 119062.
[18] J. Stursa, J. Havlik, V. Petrakova, M. Gulka, J. Ralis, V. Zach, Z. Pulec, V. Stepan, S. A. Zargaleh, M. Ledvina, M. Nesladek, F. Treussart, P. Cigler, *Carbon* **2016**, *96*, 812.
[19] J. Havlik, V. Petrakova, I. Rehor, V. Petrak, M. Gulka, J. Stursa, J. Kucka, J. Ralis, T. Rendler, S.-Y. Lee, R. Reuter, J. Wrachtrup, M. Ledvina, M. Nesladek, P. Cigler, *Nanoscale* **2013**, *5*, 3208.
[20] A. I. Shames, V. Y. Osipov, K. V. Bogdanov, A. V. Baranov, M. V. Zhukovskaya, A. Dalis, S. S. Vagarali, A. Rampersaud, *J. Phys. Chem. C* **2017**, *121*, 5232.
[21] L. J. Su, C.-Y. Fang, Y.-T. Chang, K. M. Chen, Y. C. Yu, J. H. Hsu, H. C. Chang, *Nanotechnology* **2013**, *24*, 315702.
[22] J. F. Barry, J. M. Schloss, E. Bauch, M. J. Turner, C. A. Hart, L. M. Pham, R. L. Walsworth, *Rev. Mod. Phys.* **2020**, *92*, 015004.
[23] J. Botsoa, T. Sauvage, M. P. Adam, P. Desgardin, E. Leoni, B. Courtois, F. Treussart, M. F. Barthe, *Phys. Rev. B* **2011**, *84*, 125209.
[24] F. Fávaro de Oliveira, D. Antonov, Y. Wang, P. Neumann, S. A. Momenzadeh, T. Häußermann, A. Pasquarelli, A. Denisenko, J. Wrachtrup, *Nat. Commun.* **2017**, *8*, 15409.
[25] A. I. Shames, A. I. Smirnov, S. Milikisiyants, E. O. Danilov, N. Nunn, G. McGuire, M. D. Torelli, O. Shenderova, *J. Phys. Chem. C* **2017**, *121*, 22335.
[26] P. Reineck, L. F. Trindade, J. Havlik, J. Stursa, A. Heffernan, A. Elbourne, A. Orth, M. Capelli, P. Cigler, D. A. Simpson, B. C. Gibson, *Part. Part. Syst. Charact.* **2019**, *36*, 1900009.
[27] M. Capelli, A. H. Heffernan, T. Ohshima, H. Abe, J. Jeske, A. Hope, A. D. Greentree, P. Reineck, B. C. Gibson, *Carbon* **2019**, *143*, 714.
[28] Y. Mindarava, R. Blinder, C. Laube, W. Knolle, B. Abel, C. Jentgens, J. Isoya, J. Scheuer, J. Lang, I. Schwartz, B. Naydenov, F. Jelezko, *Carbon* **2020**, *170*, 182.
[29] J. Havlik, V. Petrakova, J. Kucka, H. Raabova, D. Panek, V. Stepan, Z. Zlamalova Cilova, P. Reineck, J. Stursa, J. Kucera, M. Hruby, P. Cigler, *Nat. Commun.* **2018**, *9*, 4467.
[30] L. Dei Cas, S. Zeldin, N. Nunn, M. Torelli, A. I. Shames, A. M. Zaitsev, O. Shenderova, *Adv. Funct. Mater.* **2019**, *29*, 1970128.
[31] M. Gierth, V. Krespach, A. I. Shames, P. Raghavan, E. Druga, N. Nunn, M. Torelli, R. Nirodi, S. Le, R. Zhao, A. Aguilar, X. Lv, M. Shen, C. A. Meriles, J. A. Reimer, A. Zaitsev, A. Pines, O. Shenderova, A. Ajoy, *Adv. Quantum Technol.* **2020**, *3*, 2000050.
[32] M. D. Torelli, N. A. Nunn, Z. R. Jones, T. Vedelaar, S. K. Padamati, R. Schirhagl, R. J. Hamers, A. I. Shames, E. O. Danilov, A. Zaitsev, O. A. Shenderova, *Front. Phys.* **2020**, *8*.
[33] J. Prooth, M. Petrov, A. Shmakova, M. Gulka, P. Cigler, J. D'Haen, H. G. Boyen, M. Nesladek, *Adv. Quantum Technol.* **2023**, *6*, 2300004.
[34] K. Oshimi, H. Ishiwata, H. Nakashima, S. Mandic, H. Kobayashi, M. Teramoto, H. Tsuji, Y. Nishibayashi, Y. Shikano, T. An, M. Fujiwara, *ACS Nano* **2024**, *18*, 35202.
[35] T. Evans, S. T. Davey, S. H. Robertson, *J. Mater. Sci.* **1984**, *19*, 2405.
[36] R. M. German, *Int. J. Refract. Met. Hard Mater.* **2023**, *117*, 106401.
[37] C. A. Brookes, in *The Properties of natural and synthetic diamond*, Academic Press, London, pp. 515–546.
[38] J. D. Belnap, (Luminescent diamond) *US Patent US12325814B2*, **2022**.
[39] Y. Bao, J. D. Belnap (PCT patent application) *WO2022015780A1*, **2022**.
[40] K. C. Wong, S. L. Ng, K. O. Ho, Y. Shen, J. Wu, K. T. Lai, M. Y. Leung, W. K. Leung, D. B. R. Dasari, A. Denisenko, J. Wrachtrup, S. Yang, *Phys. Rev. Appl.* **2022**, *18*, 024044.

[41] Y. Bao, J. D. Belnap, S. N. Middlemiss, *Patent application EP2836623A1* **2015**.
[42] S. N. Middlemiss, Y. Bao, L. Carter *US Patent US9586376*, **2013**.
[43] C. M. Sung, *High Temp.–High Press.* **1997**, *29*, 253.
[44] M. Akaishi, H. Kanda, Y. Sato, N. Setaka, T. Ohsawa, O. Fukunaga, *J. Mater. Sci.* **1982**, *17*, 193.
[45] D. Wirtitsch, G. Wachter, S. Reisenbauer, M. Gulka, V. Ivády, F. Jelezko, A. Gali, M. Nesladek, M. Trupke, *Phys. Rev. Res.* **2023**, *5*, 013014.
[46] C. L. Degen, F. Reinhard, P. Cappellaro, *Rev. Mod. Phys.* **2017**, *89*, 035002.
[47] D. Bluvstein, Z. Zhang, A. C. B. Jayich, *Phys. Rev. Lett.* **2019**, *122*, 076101.
[48] I. Cardoso Barbosa, J. Gutsche, A. Widera, *Phys. Rev. B* **2023**, *108*, 075411.
[49] O. Dhungel, M. Mrózek, T. Lenz, V. Ivády, A. Gali, A. Wickenbrock, D. Budker, W. Gawlik, A. M. Wojciechowski, *Opt. Express* **2024**, *32*, 21936.
[50] E. Bauch, S. Singh, J. Lee, C. A. Hart, J. M. Schloss, M. J. Turner, J. F. Barry, L. M. Pham, N. Bar-Gill, S. F. Yelin, R. L. Walsworth, *Phys. Rev. B* **2020**, *102*, 134210.
[51] T. Irifune, A. Kurio, S. Sakamoto, T. Inoue, H. Sumiya, K. I. Funakoshi, *Phys. Earth Planet. Inter.* **2004**, *143*, 593.
[52] R. Blinder, Y. Mindarava, M. Korzeczek, A. Marshall, F. Glöckler, S. Nothelfer, A. Kienle, C. Laube, W. Knolle, C. Jentgens, M. B. Plenio, F. Jelezko, *Sci. Adv.* **2025**, *11*, eadq6836.
[53] T. Boele, D. E. J. Waddington, T. Gaebel, E. Rej, A. Hasija, L. J. Brown, D. R. McCamey, D. J. Reilly, *Phys. Rev. B* **2020**, *101*, 155416.
[54] K. Iakoubovskii, A. Stesmans, *Phys. Status Solidi A* **2004**, *201*, 2509.